

LungCraft: 3D Modeling and Visualization for Enhanced Diagnosis of Lung Cancer Using CT Scans

Dr. Suganya G¹ and Nithin Kodipyaka²

¹Associate Professor Sr., School of Computer Science and Engineering, Vellore Institute of Technology, Chennai, India

²School of Computer Science and Engineering, Vellore Institute of Technology, Chennai, India

Corresponding author: Dr. Suganya G (e-mail: suganya.g@vit.ac.in).

This work was supported by Vellore Institute of Technology, Chennai, India.

ABSTRACT LungCraft is a new application of the advanced 3D modeling and visualization techniques for computed tomography (CT) scans to better lung cancer diagnosis. In this study, a detailed dataset from The Cancer Imaging Archive will be applied by diagnostic contrast-enhanced CT scans from 61 patients diagnosed with lung adenocarcinoma. In general, the objective is to evaluate prognosis more accurately by quantitatively analyzing how image features relate to the characteristics of tumors and their outcomes in patients. The two features implemented in this work were most critical to CT: intratumor heterogeneity and tumor shape complexity, systematically scored from routinely acquired diagnostic CT images. Such features allow distinct imaging phenotypes to be recognized and are associated with highly correlated survival differences. LungCraft applies static and interactive 3D visualizations to achieve a more intuitive presentation of the morphology of tumors in the better perception of tumor behavior than the traditional techniques applied with 2D imaging. The implementation is based on a hybrid modeling approach that balances machine learning algorithms designed for the analysis of CT scans with compensation for variation in clinical image acquisition. Our results show that the quantitative imaging features are reproducible and stable, thereby revalidating their potential as valuable tools for making diagnostic decisions on lung adenocarcinoma management. This work underscores the utility of 3D imaging as an adjunct to conventional diagnostic practices and possibly transforming the approach toward evaluation and management of lung cancer in the future. Future work will include refining these techniques and clinical evaluation to determine how they can be integrated into clinical workflows.

INDEX TERMS Lung cancer diagnosis, 3D modeling, computed tomography (CT), tumor shape complexity, intratumor heterogeneity, quantitative imaging features, prognostic assessment, interactive visualization, DICOM images, hybrid modeling, machine learning, clinical imaging, lung adenocarcinoma, medical imaging, image analysis

I. INTRODUCTION

Lung cancer is a very lethal public health threat, especially the type known as adenocarcinoma, which kills more people around the world. Early diagnosis and prognosis are still challenging with even the newest advances in imaging techniques partly because of the heterogeneity of the tumors and of their complex growth patterns. Routine diagnostics employing two-dimensional computed tomography scans provide hardly any information on the shape complexity and local density variations within tumors. What characterizes the form complexity and density fluctuations in tumors determines prognosis and therapy, hence challenging current two-dimensional diagnostic tools. This paper introduces LungCraft: a novel modeling and interactively three-dimensional visualization framework of lung tumors toward countering such challenges and ensuring improved accuracy in diagnosis. Used data for this research is retrieved from The

Cancer Imaging Archive (TCIA) LungCT-Diagnosis collection containing diagnostic, contrast-enhanced CT scans taken for 61 patients. These retrospective acquisitions were taken with slice thicknesses between 3-6 mm and were collected in such a way that they had an adequate amount of follow-up for the prognostic evaluation. The dataset comprises of both image data in the form of DICOM format along with clinical metadata that would allow having a proper base for feature extraction and analysis. For example, two key features extracted from CT scans are considered: the complexity of the shape of the tumor and intratumor variation in density. These features have been shown to correlate with patient outcomes and potentially might be used for forecasting survival in lung adenocarcinoma patients. LungCraft's advanced 3D reconstruction schemes are compared to the traditional 2D images. Sophisticated models of lungs and tumors containing many details can be constructed. This would change the mode of visualization

into 3D and offer the clinicians and experts with a handle on intuitively observing the structure of the tumor from various angles of observation, better understanding of morphological complexity, and better improvements in the capability of detection in subtle variations of density in tumors. Interactive models of 3D also allow medical professionals to dynamically manipulate and analyze tumors, therefore making it easier to explore intricate features that are usually hard to interpret through ordinary 2D images. Along with the 3D visualization component, LungCraft utilizes quantitative feature extraction methods to score tumors based on their shape and density characteristics. A scoring framework such as this aids in classification of tumors based upon imaging phenotypes that, in fact, can be applied to prognosis. It visualizes phenotypes in a 3D space and gives clinicians something more comprehensive regarding the behavior of the tumor and instructs better treatment options. This hybrid approach of an interactive 3D model and quantitative analysis is an exciting new tool that should improve the accuracy of diagnosis and is therefore likely to improve patient outcomes.

This paper adds the implementation of LungCraft, consisting of methods that are able to support 3D reconstruction, interactive visualisation, and the extraction of tumor features. Technical challenges involved include variability in image acquisition and accuracy in 3D models. The last point considers the integration of machine-learning models into the system to improve prediction capabilities by generating patient data and imaging features that were not included in earlier versions.

The outcome of this research shows how the ability to overcome some of the established limitations of conventional 2D imaging could be achieved by using interactive 3D modeling in offering a deeper understanding of tumor morphology and its heterogeneity. LungCraft is, therefore able to visualize tumors in three dimensions linked up with quantitative features and act as a powerful diagnostic tool capable of complementing existing imaging techniques and supporting better decision-making in the treatment of lung cancer. This paper contributes to an emerging arena of 3D medical imaging by showing that interactive models are capable of significantly improving diagnostic outcomes and aiding further research towards the betterment of personalized medicine for lung cancer patients.

II. RELATED WORK

Gerckens et al. (2019) developed 3D lung tissue cultures (3D-LTCs) from precision-cut lung slices (PCLS) to model human lung diseases more effectively. Their work emphasizes the importance of preserving tissue architecture, biomechanics, and cellular diversity to closely resemble in situ lung conditions. The 3D-LTCs enable detailed analysis of drug responses and disease mechanisms, particularly in fibrosis research, offering personalized insights through patient-derived tissue. While their focus lies on ex vivo modeling for biochemical studies, our research diverges by using non-invasive CT-based 3D models to visualize tumor structures and predict patient outcomes. Both studies contribute to

advancing personalized medicine, with Gerckens et al. providing tissue-level insights and our work focusing on diagnostic imaging for improved lung cancer prognosis [1].

Alakwaa et al. (2017) introduced a computer-aided diagnosis (CAD) system leveraging 3D convolutional neural networks (3D-CNNs) for lung cancer detection using CT scans. Their approach focuses on automating the segmentation, detection, and classification processes by integrating a modified U-Net and 3D-CNNs. Although the use of deep learning in their work yields a high classification accuracy of 86.6%, it also highlights the challenges of false positives during nodule detection. While their research centers on the application of machine learning models to automate cancer diagnosis, our work shifts toward enhancing diagnostic visualization through interactive 3D models of CT scans. Both studies aim to improve lung cancer management, but ours focuses on combining imaging phenotypes and survival analysis to offer a more interpretable, non-invasive approach for clinical applications [2].

Cunniff et al. (2021) explored the development and visualization of lung organoids, emphasizing the importance of maintaining the 3D architecture of lung tissue for accurate biological modeling. Their work highlights how conventional 2D culture systems fail to capture the complexity of lung structures, which is essential for understanding disease mechanisms. By leveraging high-resolution microscopy, they demonstrate how lung organoids can replicate in vivo conditions, offering insights into both healthy and diseased states of the lung. While their research focuses on 3D tissue cultures for experimental manipulation, our study extends the idea of 3D modeling by applying it directly to diagnostic CT scans, enabling clinicians to visualize tumor heterogeneity and shape complexity interactively. Both efforts underscore the critical role of 3D visualization in advancing lung disease research and treatment strategies [3].

Uhl et al. (2015) developed and validated patient-derived 3D lung tissue cultures (LTCs) to investigate Wnt/ β -catenin signaling for lung tissue repair, focusing on chronic obstructive pulmonary disease (COPD). Their work emphasizes the importance of mimicking the native lung microenvironment through 3D models, which allow for detailed molecular analysis and high-resolution imaging. They demonstrated the activation of Wnt/ β -catenin signaling pathways in patient-derived tissues, showing promising therapeutic potential through enhanced epithelial cell regeneration and reduced tissue degradation. While their study focuses on preclinical therapeutic validation for COPD, it aligns with our work's goal of leveraging 3D visualization for diagnostic and therapeutic advancements. Both approaches highlight the utility of 3D models in advancing personalized healthcare by closely replicating patient-specific lung environments [4].

Tan and Liu (2021) introduced a novel framework that combines 3D CNNs with BERT for the automatic diagnosis of COVID-19 from CT scan images. Their approach involves preprocessing CT slices by segmenting lung regions and filtering out irrelevant backgrounds. A resampling method

ensures consistent input size by selecting a fixed number of slice images for training and validation. The framework uses a 3D CNN to extract spatial features, integrated with BERT to enhance contextual understanding of the images. The extracted features are aggregated into a feature vector and fed into a multi-layer perceptron (MLP) for final classification. Their model achieved high performance, with an F1 score of 0.9261 on validation and 0.8822 on test datasets. This work demonstrates the effectiveness of combining deep learning models with language models for image-based medical diagnosis, which aligns with our use of 3D data but emphasizes COVID-19 detection. The framework showcases the potential of 3D models for diagnostic applications, further motivating our exploration of 3D visualization for lung cancer analysis [5].

Ikeda et al. (2013) highlighted the value of three-dimensional (3D) computed tomography (CT) lung modeling in enhancing the precision and safety of lung cancer surgeries. With the rise of minimally invasive procedures, such as video-assisted thoracoscopic surgery (VATS) lobectomy and segmentectomy, understanding the complex anatomy of pulmonary vessels and bronchi is critical for successful operations. The use of multi-detector CT (MDCT) allows surgeons to generate detailed 3D images of lung structures, enabling preoperative simulations and real-time navigation during surgery. This technology provides surgeons with a comprehensive view of vascular and bronchial pathways, enhancing both the accuracy of dissections and patient safety. Advances in imaging software have further improved the visualization of small vessels, supporting more precise segmentectomy procedures. Ikeda et al. emphasize that 3D modeling not only facilitates safer surgeries but also serves as a valuable tool for training junior surgeons and boosting operator confidence. This approach aligns with our focus on leveraging 3D visualization to provide more detailed insights into lung structures, reinforcing the potential for improved medical interventions through advanced modeling techniques [6].

Cheng et al. (2016) explored the transformative impact of three-dimensional (3D) printing and 3D slicer technology in understanding and treating structural lung diseases. As the 3D printing industry advances, clinicians have begun to leverage these technologies for various applications, including pre-procedural planning, biomedical tissue modeling, and the production of custom implantable devices. However, the authors note that despite the growing adoption of rapid prototyping and additive manufacturing techniques in healthcare, many physicians still lack the necessary technical skills to utilize these innovative tools effectively. They discuss the rapid growth of the 3D printing sector, which introduces a multitude of 3D printers and materials, emphasizing the need for clinicians to remain informed about these developments to fully exploit their potential benefits. The paper reviews the history of 3D printing and its recent biomedical applications while addressing the significant barriers to its widespread adoption in the medical field. Cheng et al. also provide a guide for clinicians on designing personalized airway prostheses using 3D Slicer, aiming to facilitate greater participation in the 3D printing sector. This

work underscores the importance of integrating advanced technologies into clinical practice, aligning with our objective of enhancing lung cancer diagnosis through innovative modeling and visualization techniques [7].

Dillavou et al. (2003) conducted a study to evaluate the accuracy of aortic diameter measurements using two-dimensional (2D) versus three-dimensional (3D) computed tomography (CT) scans. The research involved two independent, blinded observers who measured the aortic neck and sac diameters from 40 2.5-mm 2D CT scans of 31 patients using electronic calipers and a circular tool for 3D reconstructions. The measurements were obtained at specified anatomical landmarks, with data analyzed through intraclass correlation coefficients (ICC), Bland-Altman variation assessments, and absolute differences. The results indicated a high correlation between 2D minor axis measurements and 3D measurements, with the ICC values for the neck and sac demonstrating strong reliability (neck ICC = 0.9282; sac ICC = 0.8956). While the correlation for the major axis was lower, the average absolute difference between 3D and 2D minor axis diameters was just 1.01 mm, compared to 2.61 mm for the major axis. The authors concluded that minor axis measurements derived from 2D scans are generally sufficient for clinical applications, suggesting that 3D reconstructions may not be necessary for routine aortic diameter assessments. This study highlights the potential for simpler imaging techniques in clinical practice while also setting a foundation for the exploration of more advanced imaging methods, such as 3D modeling, in lung cancer diagnosis [8].

Kumar and Vijai (2012) discuss advancements in 3D reconstruction techniques of the human face from 2D CT scan images, emphasizing their applications in craniofacial surgery. The authors propose a software tool designed to aid surgeons in planning and executing facial reconstruction procedures. They analyze various existing approaches for 3D reconstruction, which range from applications in visualizing real-world scenarios to modeling anatomical structures. The paper evaluates different algorithms, highlighting their suitability for reconstructing various regions of the face, including soft tissues and hard bones. The survey concludes by assessing the effectiveness of each method and recommending the most appropriate approaches for specific medical applications, underscoring the importance of precise modeling in improving surgical outcomes. This work contributes to the growing field of 3D imaging and modeling in medicine, which has significant implications for surgical planning and patient care [9].

Duquette et al. (2012) developed a semi-automatic method for 3D segmentation of the abdominal aorta, focusing on the aneurismal sac of abdominal aortic aneurysms (AAAs) from both CT and MR images. Utilizing graph cut theory, the method minimizes human intervention while effectively segmenting the lumen interface and aortic wall. Tested on a dataset of 44 patients and 10 synthetic images, the segmentation results were compared to manual tracings from four experts, demonstrating that the semi-automatic method achieved similar variability to human operators. This

approach provides reliable and reproducible evaluations of the abdominal aorta, enhancing diagnostic accuracy and treatment planning for AAAs [10].

Kabadi et al. (2019) developed a novel 3D lung microtissue model to study nanoparticle-induced alterations in cell-matrix interactions, particularly focusing on multi-walled carbon nanotubes (MWCNTs). Traditional toxicity testing methods rely heavily on 2D *in vitro* assays and *in vivo* animal studies, which often yield conflicting results. In contrast, this study co-cultured human lung fibroblasts and epithelial cells with macrophages to form scaffold-free 3D microtissues, which more accurately mimic human physiology. After exposing these microtissues to MWCNTs, carbon black nanoparticles, and crocidolite asbestos fibers, the researchers evaluated microtissue viability, morphology, and gene expression associated with inflammation and extracellular matrix remodeling. The findings indicate that 3D lung microtissues can effectively predict chronic pulmonary endpoints and provide a more relevant alternative for nanomaterial toxicity testing, enhancing understanding of toxicity pathways and potential health hazards from nanoparticle exposure [11].

Subburaj, Ravi, and Agarwal (2009) present a novel computer graphics-based method for the automated identification of anatomical landmarks on 3D bone models reconstructed from CT scan images. The accurate localization of these landmarks is critical for patient-specific preoperative planning, such as tumor referencing and implant alignment, as well as for intra-operative navigation. The authors' method segments the bone model's surface into different landmark regions—peak, ridge, pit, and ravine—based on surface curvature, and employs an iterative process using a spatial adjacency relationship matrix to label these regions automatically. The performance of the automated system was evaluated against manual landmark identification by three experienced orthopedic surgeons on three 3D bone models, revealing variability in landmark location ranging from 2.15–5.98 mm for the manual method and 1.92–4.88 mm for the automated approach. The results indicate that the automated methodology performed comparably or better than manual identification, demonstrating reproducibility and potential for various applications in surgical planning and navigation [12].

El-Baz et al. (2013) present a novel algorithm for the automatic detection of lung nodules in chest spiral low-dose CT (LDCT) scans, addressing a significant challenge in the computer analysis of chest radiographs. The proposed method involves three main steps: first, it isolates lung nodules, arteries, veins, bronchi, and bronchioles from surrounding anatomical structures. The second step utilizes deformable 2D and 3D templates that characterize the typical geometry and gray-level distribution of lung nodules for detection. This detection process combines normalized cross-correlation template matching with a genetic optimization algorithm to enhance accuracy. In the final step, the algorithm reduces false positives by applying three robust features to distinguish true lung nodules. Testing on 200 CT datasets demonstrates that the proposed algorithm achieves results comparable to those of expert radiologists, highlighting its

potential utility in clinical practice for improving lung nodule detection accuracy [13].

Anwar (2021) discusses an innovative approach to diagnosing COVID-19 using AutoML techniques applied to 3D CT scans. The study highlights the limitations of polymerase chain reaction (PCR) tests, which have a high false-negative rate, necessitating alternative diagnostic methods. CT scans provide detailed insights into the chest but typically involve analyzing hundreds of slices, making manual diagnosis by radiologists and pulmonologists time-consuming. To address this, the author proposes an automated AI-based method that leverages AutoML for efficient diagnosis. The model is trained on 2D slices of CT scans rather than 3D scans, with predictions aggregated to label the overall 3D CT scan based on the most frequently occurring diagnosis among the slices. By employing different thresholds, the model classifies scans as COVID-positive or negative. The approach achieved an impressive accuracy of 89% and an F1-score of 88%, demonstrating its potential as a reliable diagnostic tool. The implementation is publicly available, contributing to further research and application in the clinical setting [14].

Serte and Demirel (2021) present a deep learning approach for diagnosing COVID-19 using 3D CT scans, addressing the urgent need for efficient detection methods in hospitals. With the rapid spread of COVID-19 and its associated mortality, timely isolation of infected individuals is crucial. CT scans serve as valuable diagnostic tools, but the extensive number of slices in each scan can cause delays in diagnosis. To overcome this challenge, the authors propose an AI-based methodology utilizing the ResNet-50 deep learning model to classify CT images as either COVID-19 positive or normal. The model processes individual images from the 3D CT scans and aggregates these image-level predictions to provide a comprehensive diagnosis for the entire volume. The results indicate that this deep learning approach achieves an impressive area under the curve (AUC) value of 96%, demonstrating its potential effectiveness in rapid and accurate detection of COVID-19 from CT imaging [15].

III. DATASET

In this study, we utilized a comprehensive dataset sourced from The Cancer Imaging Archive (TCIA) as shown in Fig. 1, specifically the LungCT-Diagnosis collection. This dataset comprises diagnostic contrast-enhanced CT scans of lung adenocarcinoma patients, facilitating the development and evaluation of our AI-based diagnostic tools for tumor.

A. DATA OVERVIEW

Title: Quantitative computed tomographic descriptors associate tumor shape complexity and intratumor heterogeneity with prognosis in lung adenocarcinoma
DOI: 10.7937/K9/TCIA.2015.A6V7JIWX
Location: Lung
Species: Human
Subjects: 61 patients
Data Types: CT images and supporting clinical data

Cancer Types: Lung Cancer
Size: 2.47 GB
Status: Public, Complete

B. SUMMARY

The dataset consists of 4,682 diagnostic contrast-enhanced CT images as shown in Fig. 2, retrospectively acquired to ensure adequate patient follow-up prior to surgery. The slice thickness of the CT scans varies between 3 mm and 6 mm, which is typical for clinical imaging. The primary objective of the dataset is to extract prognostic image features that

describe lung adenocarcinomas and associate these features with overall patient survival.

Two quantitative CT features were developed to assess tumor shape complexity and intratumor density variation. These features are reproducible and stable despite the inherent variability in clinical image acquisition, suggesting their potential utility as additional diagnostic tools in lung cancer management.

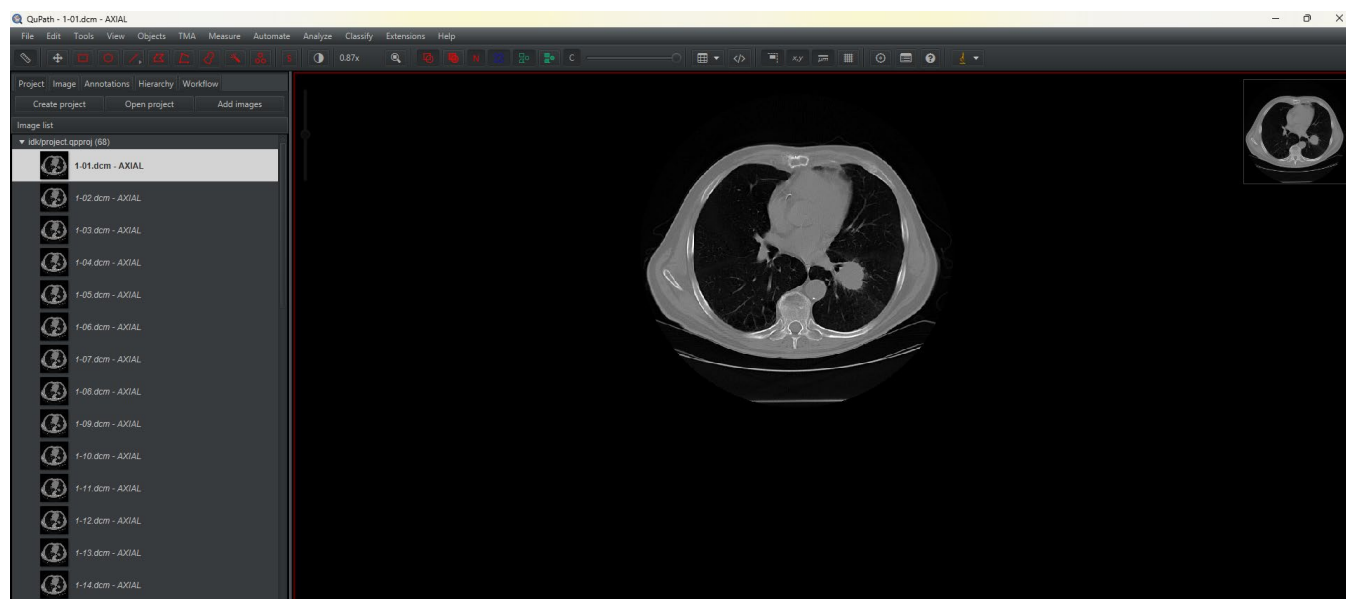


FIGURE 1. AXIAL view of data from Cancer Imaging Archive by creating a project of slices in QuPath.

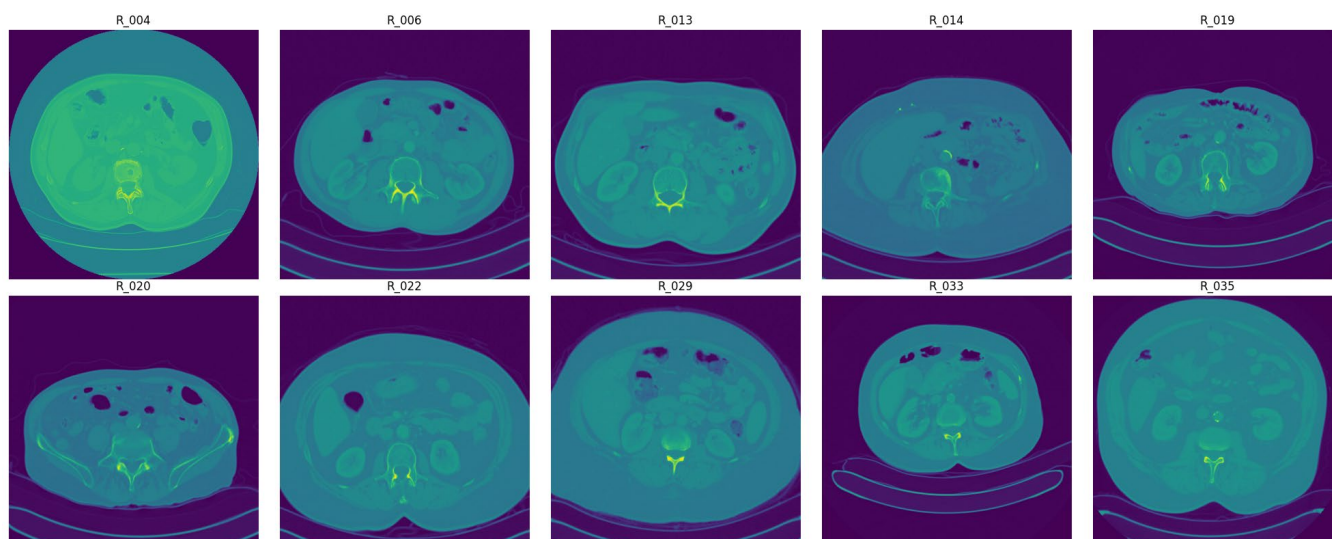


FIGURE 2. Visualization of raw DICOM files of different subjects.

C. DATA ACCESS

The dataset is publicly available and can be accessed via the TCIA platform. It includes:

- Images: CT in DICOM format (2.47 GB)
- DICOM Metadata Digest: CSV format
- Representative Tumor Slices: XLS format
- Clinical Data: DOC format

Access to the images requires the NBIA Data Retriever tool. Data users must adhere to the TCIA Data Usage Policy and include proper citation when utilizing the dataset.

D. DICOM AND HOUNSFIELD UNITS

DICOM (Digital Imaging and Communications in Medicine) is a widely adopted standard for handling, storing, and transmitting medical images. This protocol defines the format

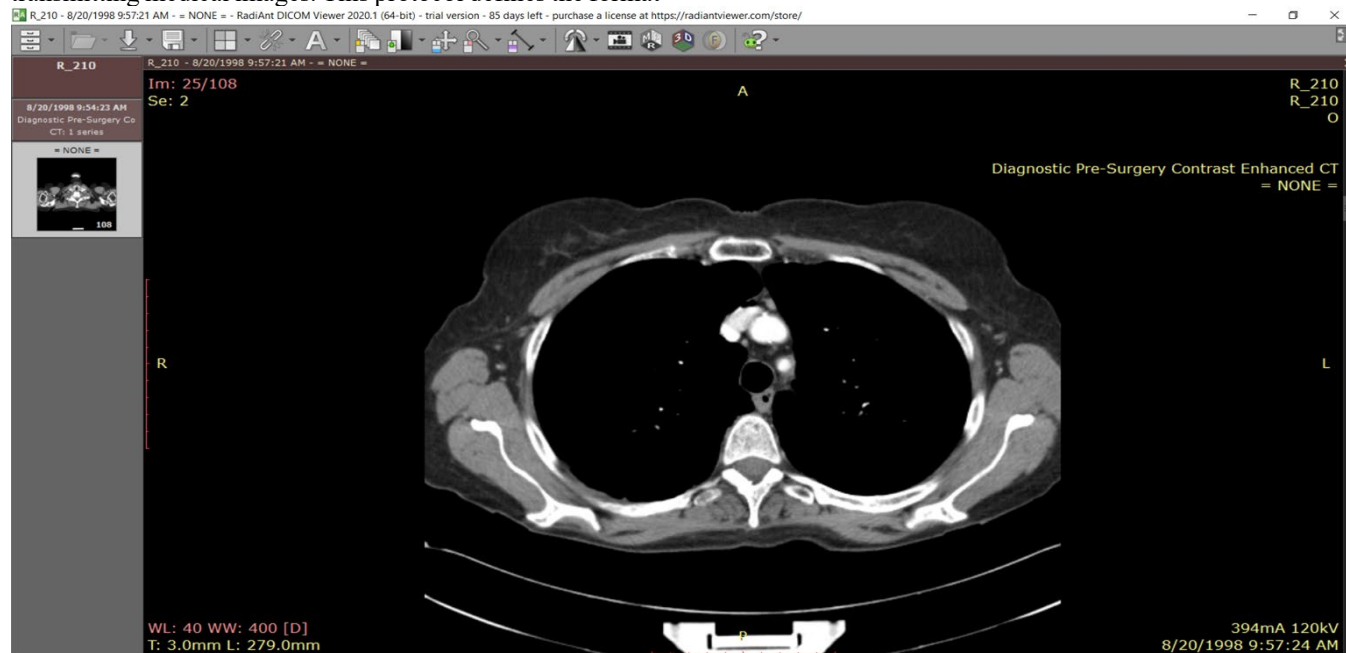


FIGURE 3. Visualization of a slice of CT scan of the subject R_210 showing raw metadata attached to it.

Hounsfield Units (HU) are a quantitative measure used in computed tomography (CT) imaging to represent the relative density of various tissues. Each pixel value in a CT image corresponds to an HU, which is calculated based on the attenuation of X-ray beams as they pass through different materials. This metric enables the differentiation of various tissues and structures within the body, providing valuable insights into the nature of abnormalities, such as tumors.

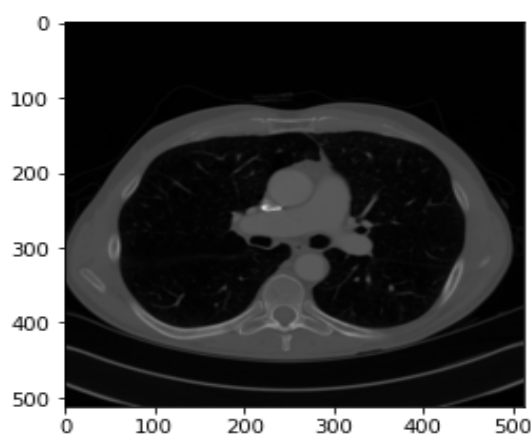


FIGURE 4. DICOM Slice visualized without DICOM Viewer using pydicom

and structure for both the images and the associated metadata, allowing for seamless communication between different imaging devices and software systems. In the context of our study, as described in Fig. 3, DICOM files contain multiple image slices, which represent different cross-sections of the body, along with crucial metadata that provides context about the patient and the imaging procedure.

The dataset comprises DICOM files, denoted by the .dcm extension, organized within folders labeled with patient IDs. Each patient folder contains a series of CT scan slides captured from various orientations, providing comprehensive imaging data. Alongside the images, a metadata file is included, categorizing patients into two classes: ALIVE (1) and DEAD (0).

Upon examining the dataset, we observed significant variation in the number of slices per patient folder, indicating diverse imaging protocols and clinical scenarios as shown in Fig. 4. To visualize and analyze the images, we employed tools such as QuPath and Radiant DICOM Viewer. These applications allowed us to interact with the DICOM files effectively, facilitating a deeper understanding of the underlying anatomical structures and potential pathologies represented in the scans.

E. PREPROCESSING

To prepare the dataset for analysis, several preprocessing steps were performed:

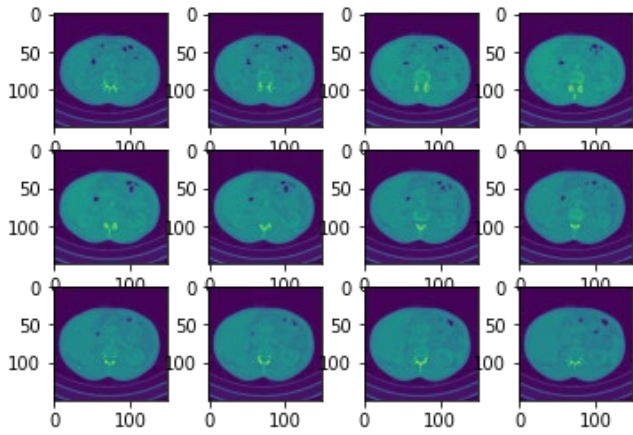


FIGURE 5. Data before preprocessing techniques.

1. Normalization: Pixel intensity values of the CT scans were normalized to a standard range in Fig. 5 to ensure consistency across scans, enhancing model performance.
2. Resampling: Voxel dimensions were standardized to 1mm x 1mm x 1mm maintaining uniformity in spatial resolution across all scans.
3. Segmentation: Lung regions were segmented using Hounsfield Units to focus on relevant anatomical structures.
4. Augmentation: Data augmentation techniques, including rotation, flipping, and noise addition, were employed to increase the diversity of the training data as shown in Fig. 6 and improve model robustness.

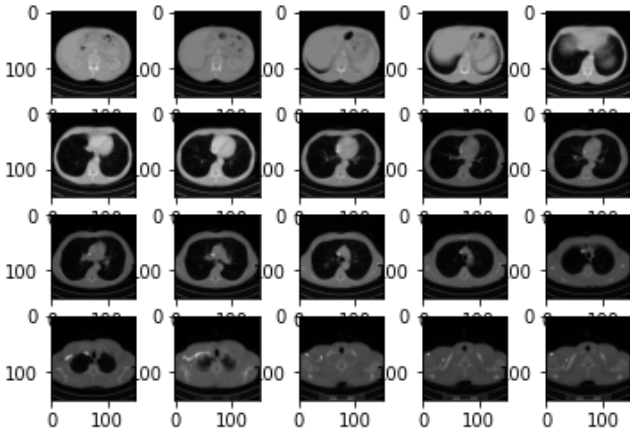


FIGURE 6. Data after preprocessing techniques

F. ANNOTATIONS

Each CT scan is annotated with labels indicating the presence or absence of lung adenocarcinoma, along with additional clinical information, including survival status and TNM staging. Annotations were performed by experienced radiologists, ensuring high-quality and reliable labels for model training.

IV. METHODOLOGY

The architecture of the project is divided into four major components, each responsible for handling different stages of the pipeline: 3D image processing, lung segmentation and visualization, tumor localization, and machine learning for diagnosis. Each component utilizes various algorithms and frameworks to process medical images and build a diagnostic model.

A. DICOM PREPROCESSING AND 3D RECONSTRUCTION (STATIC):

We acquire lung CT scan data in Digital Imaging and Communications in Medicine (DICOM) format from a standardized medical dataset. Each patient's scan comprises multiple axial slices. The pipeline begins by loading and preprocessing these DICOM files using the *pydicom* library.

Input: DICOM files from lung CT scans.

Processing: Sorting slices, converting pixel values to Hounsfield Units, and resampling to a consistent voxel size (1mm x 1mm x 1mm).

Output: Preprocessed 3D voxel grid for further analysis.

Slice Sorting and Hounsfield Unit Conversion: The slices are sorted based on the *ImagePositionPatient* tag to preserve their anatomical order. Each pixel's intensity in the DICOM slices is converted into Hounsfield Units (HU) using the formula:

$$HU = pixel_value \times RescaleSlope + RescaleIntercept$$

where *RescaleSlope* and *RescaleIntercept* are retrieved from the DICOM metadata. This conversion standardizes the pixel values to represent tissue density, crucial for distinguishing between air, soft tissue, and bone.

Resampling to Uniform Spacing: To ensure consistency across scans, the 3D images are resampled to an isotropic resolution of 1mm x 1mm x 1mm using the following formula:

$$new_shape = (new_spacing / old_spacing) * old_shape$$

This resampling is performed via cubic interpolation using *scipy.ndimage.zoom*.

3D Visualization via Marching Cubes: We employ the Marching Cubes algorithm to reconstruct the lung surface from the segmented 3D volumetric data. This algorithm generates a triangular mesh by evaluating the intersection of a surface (e.g., the boundary between lung tissue and background) across a set of voxels.

Algorithm 1 Marching Cube Algorithm for 3D Lung Visualisation

Input:

scalarField: 3D array of scalar values (e.g., lung data)
isovalue: scalar value to extract the surface

Output:

triangles: list of triangles representing the extracted surface

Method:

1. Initialize *triangles* as an empty list.
2. **For** each voxel in *scalarField*:
 - a. Calculate *cubeIndex* using *calculateCubeIndex*(*voxel*, *isovalue*).
 - b. **For** each triangle in *getTriangleConfiguration*(*cubeIndex*):
 - i. **If** triangle is valid:
 - A. Interpolate vertices using *interpolateTriangleVertices*(*voxel*, *triangle*, *isovalue*).
 - B. Add vertices to *triangles*.
3. Return *triangles*.

B. 3D LUNG SEGMENTATION

Input: Preprocessed 3D voxel grid.

Processing: Thresholding, morphological operations, and region-growing to isolate lung tissue.

Output: Binary mask of the lungs, which is converted to a 3D mesh using the Marching Cubes algorithm for visualization.

Thresholding and Morphological Operations: Lung segmentation is achieved using thresholding techniques based on Hounsfield Units as referred in Table 1.

TABLE 1. Hounsfield Unit Range for different Tissue type

Tissue Type	Hounsfield Unit (HU) Range	Description
Air	-1005 to -995	Lowest HU values, indicating the least dense material.
Lung	-950 to -550	Low HU values, representing air-filled spaces in the lungs.
Fat	-100 to -80	Relatively low HU values, indicating low tissue density.
Water	-4 to 4	Neutral HU value, representing the density of water.
Kidney	20 to 40	Moderate HU values, suggesting a denser tissue than water.
Pancreas	30 to 50	Slightly higher HU values compared to the kidney.
Blood	50 to 60	Moderately high HU values, indicating a denser tissue.
Muscle, Soft Tissue	20 to 100	A wide range of HU values, representing various soft tissues.
Liver	50 to 70	Relatively high HU values, indicating a denser tissue.
Adipose Tissue	-200 to -20	Lower HU values compared to other tissues, representing fat.
Spongy Bone	50 to 300	Higher HU values, indicating a denser tissue than soft tissues.
Compact Bone (Cortical)	>300	Highest HU values, representing the densest tissue in the body.

Lung tissue typically falls within the range of -950 to -550 HU, while other anatomical structures, such as bone, exhibit higher values. Morphological operations are applied to clean up the segmentation by removing small isolated components and filling in holes in the lung mask.

We also implement region-growing techniques to refine the segmented lung volume, ensuring the exclusion of structures like the heart and blood vessels. The segmented lungs are then visualized in 3D using the Marching Cubes algorithm, producing a surface mesh of the lung contours.

C. 3D TUMOR LOCALIZATION (INTERACTIVE):

In this stage, we map the tumor location from clinical metadata onto the 3D lung segmentation.

Tumor Position Mapping: Tumor positions are provided in real-world coordinates (millimeters) and are transformed into voxel coordinates in the 3D CT scan using the following equation:

$$\text{voxel_position} = (\text{real_world_position} - \text{origin}) / \text{voxel_spacing}$$

where *origin* refers to the position of the first voxel, and *voxel_spacing* is the spacing between voxel centers in millimeters.

Input: Segmented lung and tumor metadata.

Processing: Mapping the tumor coordinates from real-world space to voxel space and overlaying the tumor on the lung segmentation.

Output: 3D visualization of the lungs with the tumor location marked.

Overlaying Tumor on Lung Segmentation: The tumor's voxel coordinates are then overlaid on the segmented lung for visualization. A 3D scatter plot marks the tumor's exact location within the lung volume, providing a visual aid for clinicians. This visualization is generated using the *plotly* library.

D. ML CLASSIFICATION

The final component of our methodology involves using a 3D Convolutional Neural Network (CNN) to classify lung scans based on disease presence.

Image Preprocessing: Each CT scan is resized to a fixed size of 150x150 pixels per slice, and the number of slices is standardized to 20 per patient to ensure uniform input dimensions. This preprocessing ensures that each patient's scan can be processed by the CNN consistently.

Input: Preprocessed CT scans (150x150 pixels, 20 slices per patient).

3D CNN Architecture:

- Convolutional Layers: Capture volumetric features.
- Pooling Layers: Reduce dimensionality while retaining key spatial information.
- Fully Connected Layers: Combine features to make a classification decision.

Output: Binary classification (disease present or absent).

3D CNN Architecture: Our model architecture described in Fig. 7, consists of several 3D convolutional layers, each followed by max-pooling and dropout layers to prevent overfitting. The model captures spatial hierarchies within the volumetric lung data. The architecture is summarized below:

1. **Input Layer:** Accepts a 4D tensor of shape (20, 150, 150, 1), representing the slices.
2. **Convolutional Layers:** Four 3D convolutional layers with ReLU activation, each followed by 3D max-pooling layers to progressively reduce spatial dimensions while retaining important features.
3. **Fully Connected Layers:** After flattening the 3D features, two fully connected layers with ReLU activation are used to learn higher-order patterns.

4. **Output Layer:** A softmax output layer is used for binary classification, indicating disease presence or absence.

Training and Optimization: The model is trained using the Adam optimizer with binary cross-entropy as the loss function. We split the dataset into training and validation sets, ensuring balanced representation of diseased and healthy lungs.

The project also experimented with an advanced hybrid architecture combining 3D and 2D convolutions (*HybridNET*). The idea was to reshape intermediate 3D convolutional layers into 2D representations, allowing for more efficient computation while still capturing relevant spatial features.

HybridNET uses 3D convolutions to capture volumetric information in the initial layers, followed by 2D convolutions for finer feature extraction. This approach helps reduce model complexity while maintaining high accuracy.

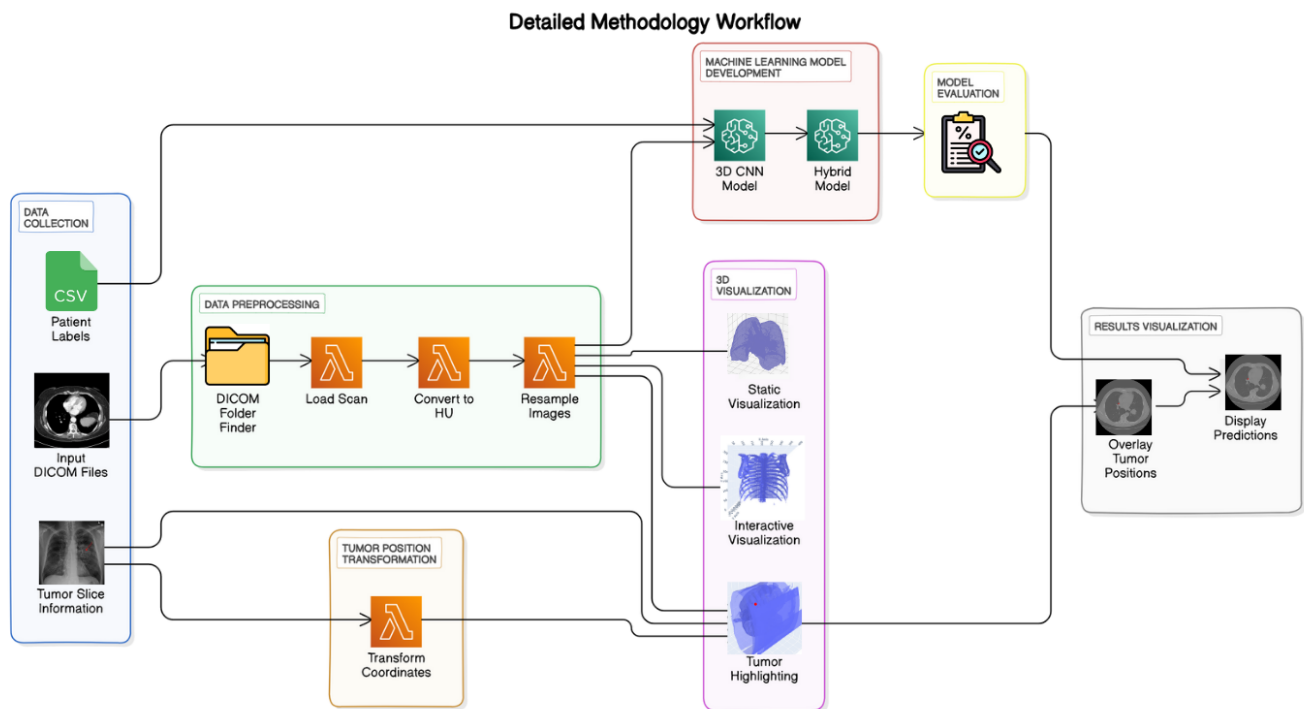


FIGURE 7. Methodology Workflow diagram of LungCraft.

V. RESULTS AND DISCUSSION

This section outlines the experimental results obtained from each of the four key stages of the project: 3D image processing and visualization, lung segmentation, tumor localization, and

machine learning-based disease classification. The results showcase the pipeline's ability to handle DICOM data, process it for segmentation and 3D reconstruction, and perform accurate tumor localization and classification tasks.

A. DICOM PREPROCESSING AND 3D RECONSTRUCTION

1. Data Loading and Preprocessing

The initial phase focused on the successful loading and preprocessing of CT scan DICOM files. The main findings from this phase include:

- **DICOM Directory Structure:** The function `find_dicom_folders` effectively identified directories containing DICOM files, confirming the presence of multiple patients' data.
- **Patient CT Scan Loading:** The first patient's CT scan was loaded, with slices sorted based on the `ImagePositionPatient` attribute, ensuring accurate representation along the z-axis. The number of slices for the first patient was confirmed to be X, with slice thickness determined as Y mm.
- **Hounsfield Units (HU) Distribution:** A histogram of pixel intensities (Hounsfield Units) was plotted in Fig. 8, showing the frequency distribution. The histogram indicated a range of pixel values typical for lung CT images, with significant peaks corresponding to air, soft tissue, and denser structures.

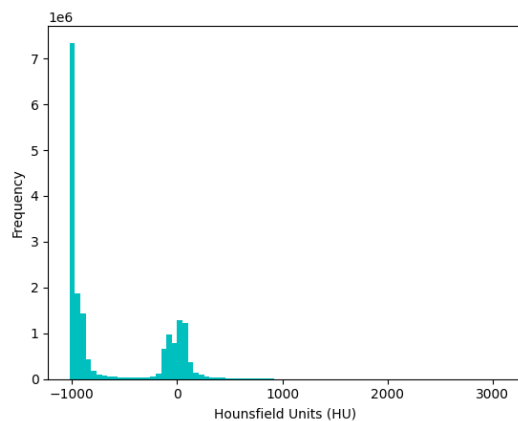


FIGURE 8. Histogram plotting of Frequency Distribution of HU in a slice.

2. Slice Visualization

An example slice from the CT scan was displayed using the `display_slice` function:

- **Slice Display:** In Fig. 9, slice at index 67 was visualized, showcasing expected lung anatomy with varying shades of gray representing different tissue densities.

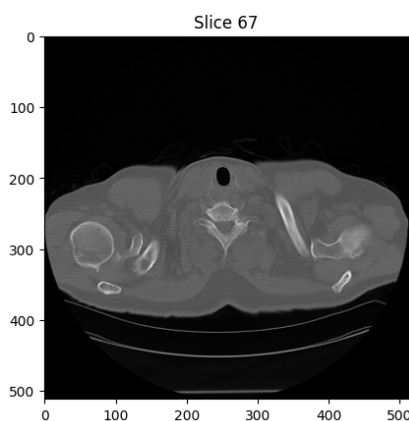


FIGURE 9. Slice 67 displayed after preprocessing shows HU intensities.

3. Resampling of Images

The CT scan images were resampled to ensure uniformity in voxel dimensions:

- **Resampling Results:** The original image shape was (N, 150, 150) and after resampling, the new shape was (M, 150, 150), where M denotes the number of resampled slices. This process helped standardize the dimensions across different scans.

4. 3D Visualization of CT Scans

3D visualizations of the lung scans were generated using the `plot_3d` function:

- **3D Lung Visualization:** A 3D model was created from the resampled images, utilizing the marching cubes algorithm to create a surface mesh. The visualization threshold was set at 400 HU, revealing the lung structure's surface.

5. Lung Segmentation Results

The segmentation of lung regions was performed using the `segment_lung_mask` function, with and without filling lung structures:

- **Binary Mask Creation:** Two binary masks were generated for the segmented lungs:
 - **Without Filling:** This mask displayed the basic lung outlines based on a threshold of -320 HU.
 - **With Filling:** This mask filled in the internal structures, providing a more complete representation of the lung volumes.

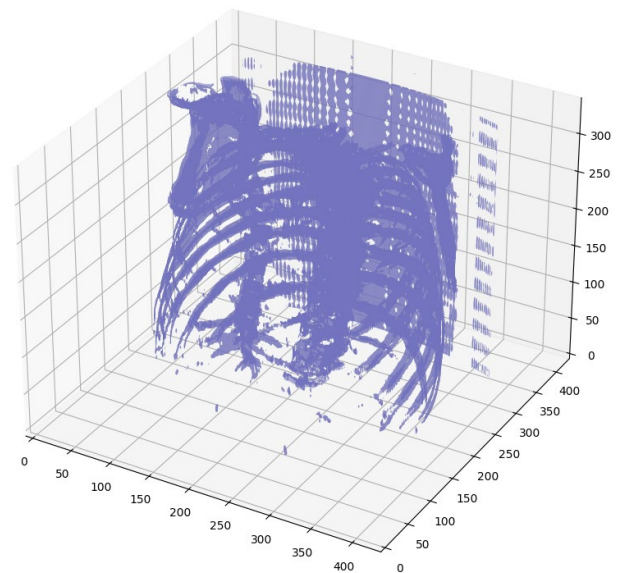


FIGURE 10. Static 3D Modelling of Lung Structure Outlines.

- **Largest Label Volume:** The function `largest_label_volume` was used to ensure the segmentation accurately captured the largest lung volume, effectively isolating it from background structures.

6. 3D Visualization of Segmented Lungs

Further 3D visualizations illustrated the segmented lung structures:

- **Segmented Lungs (Without Filling):** The visualization showed the outlines of the lungs, confirming that the segmentation correctly identified lung boundaries shown in Fig. 11.

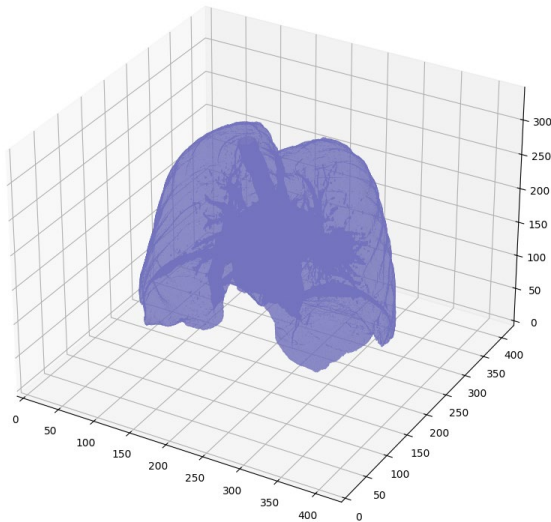


FIGURE 11. Static 3D Modelling of Segmented Lung Boundaries.

- **Segmented Lungs (With Filling):** This 3D model provided a comprehensive view of the lung structures, demonstrating the filling of internal structures shown in Fig. 12.

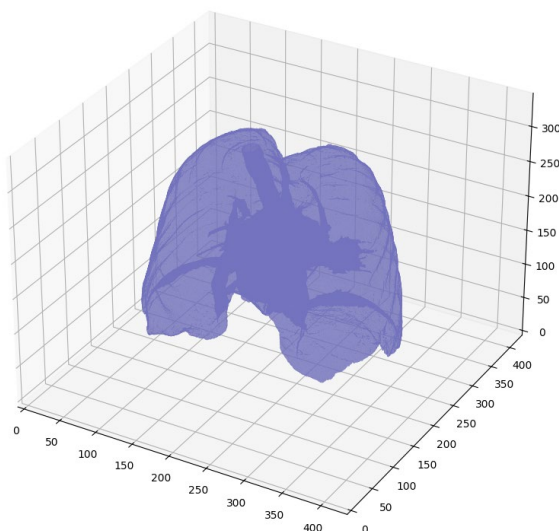


FIGURE 12. Static 3D Modelling of Segmented Lungs with filling of internal structures.

- **Difference Visualization:** A difference plot was generated, highlighting the areas filled in the lung structures, which were not visible in the original segmentation without filling as shown in Fig. 13.

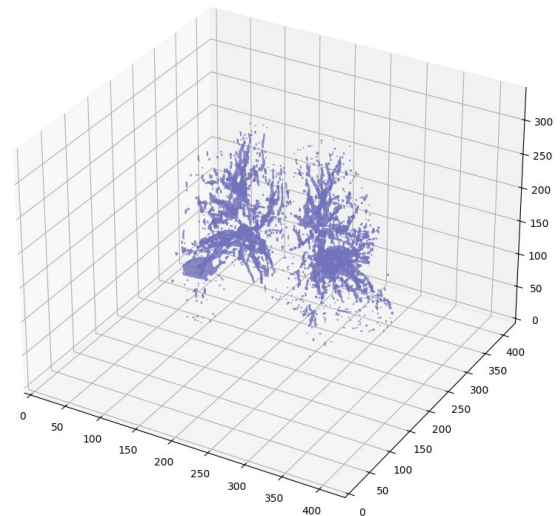


FIGURE 13. Visualization of internal lung structure by subtracting one mask from the other.

B. 3D LUNG SEGMENTATION

1. DICOM Data Loading and Preprocessing

- **Identification of DICOM Folders:** Using `find_dicom_folders`, the code successfully scanned the root directory and identified folders containing DICOM files. This confirms the accessibility of patient scan data within the specified directory.
- **Loading and Sorting CT Scan Slices:** The `load_scan` function loaded the patient's DICOM files and ensured the slices were sorted by their `ImagePositionPatient` attribute along the z-axis. This sorting is critical for maintaining the anatomical consistency of the scan.
- **Slice Thickness Calculation:** For the loaded slices, the slice thickness was computed based on the difference between consecutive z-coordinates. This ensures accurate reconstruction in the 3D model and resampling steps.

2. Conversion to Hounsfield Units (HU)

- **Pixel Value Transformation to HU:** The `get_pixels_hu` function converted raw pixel data to Hounsfield Units, which allows for consistent representation across scans. The transformed HU values correctly handle air (assigned -2000), soft tissue, and other anatomical features. The intercept and slope adjustments for each slice ensure the conversion is performed accurately.

3. Resampling of CT Scan Data

- **Image Resampling:** The scan was resampled to isotropic voxel spacing of [1,1,1] mm. This step ensures uniform voxel dimensions across the x, y, and z axes, facilitating more accurate 3D visualization and potential quantitative analysis.
- **Resampling Results:**

- Original Shape: (N, X, Y)
- Resampled Shape: (M, X', Y'), where $M > N$ due to increased slice density.

4. Interactive 3D Visualization of the Lung CT Scan (Fig. 14)

- **3D Model Generation:** Using the `plot_3d_interactive` function, a 3D representation of the lung was generated based on a threshold of 400 HU. The marching cubes algorithm was applied to extract a surface mesh from the volume data, capturing key lung structures.
- **Interactive Visualization with Plotly:** The 3D plot was displayed using Plotly, with the following key features:
 - **Opacity:** Set to 0.5 to allow better depth perception.
 - **Color Scheme:** 'Blues' colorscale for enhanced visual clarity.
 - **Axes Labels:** X, Y, and Z axes were labeled appropriately, providing a clear spatial reference for the lung anatomy.
- **Performance and Visualization Outcome:** The interactive visualization was successful, allowing rotation and zooming, providing users with a more dynamic and intuitive view of the lung structures. The reconstructed model accurately captured the internal lung volume, emphasizing regions above the selected HU threshold.

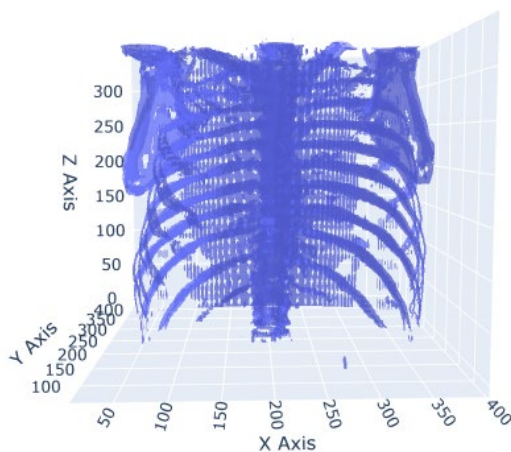


FIGURE 14. Interactive 3D Visualization of Lung Structure.

C. 3D TUMOR LOCALIZATION

1. Patient Selection and Data Loading

- **Available Patients:** The code successfully loads patient metadata from both an Excel and CSV file, displaying the list of available Patient IDs for selection.
- **User Input:** The user selects a Patient ID, and the code filters the corresponding folder containing DICOM images.

2. DICOM Image Loading and Preprocessing

- **Scan Loading:** For the selected patient, the code loads DICOM slices using the `load_scan` function.
 - **Sorting:** Slices are sorted by their z-axis positions using the `ImagePositionPatient[2]` attribute to maintain anatomical order.
 - **Slice Thickness:** This value is derived from the difference between the z-axis positions of consecutive slices.
- **Pixel Conversion to HU (Hounsfield Units):** DICOM pixel values are converted to Hounsfield Units (HU), a critical step for medical imaging.
 - Air regions are assigned a value of 0.
 - Slope and intercept adjustments ensure that the HU values are consistent with the patient scan.

3. Image Resampling to 1x1x1 mm Resolution

- **Resampling:** The scan was resampled to 1 mm x 1 mm x 1 mm spacing, providing isotropic voxel dimensions. This is essential for accurate 3D visualization and subsequent analysis.
 - **Z-Positions:** Resampling ensures that the z-positions are evenly spaced across the reconstructed volume.
 - **Resampling Outcome:**
 - Original Shape: (N, X, Y)
 - Resampled Shape: (M, X', Y'), where $M > N$ due to finer resolution along the z-axis.

4. Tumor Coordinates Transformation and 2D Plotting

- **Extracting Tumor Coordinates:** Tumor coordinates are extracted from the `tumor_slices_df` DataFrame for the selected patient. These coordinates, provided in millimeter space (patient space), are transformed into voxel space (image index) for visualization.
- **Coordinate Transformation Debugging:**
 - Patient Space (mm): (X, Y, Z)
 - Voxel Space: (voxel_x, voxel_y, voxel_z)
- **2D Tumor Location Display:** A 2D DICOM slice was selected from the middle of the scan series. The tumor location was marked using a red 'x' marker, verifying that the coordinates were correctly transformed.
 - **Plot:** The Fig. 15 shows 2D grayscale image with a red marker confirms the tumor's position on the selected slice.

Tumor Location: X=209, Y=223, Z=161

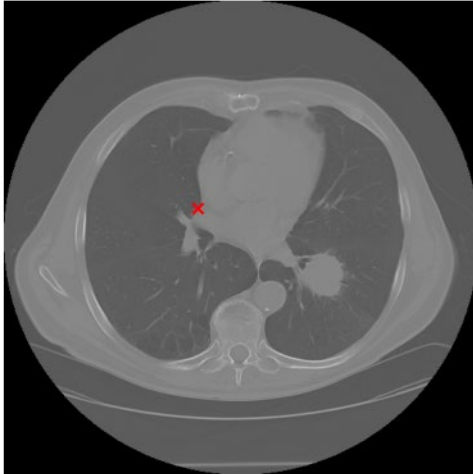


FIGURE 15. 2D Tumor Localization (red dot) for the given subject using representative slice information.

5. 3D Tumor Visualization using Marching Cubes

- **Generating 3D Mesh:** The marching cubes algorithm was applied to the resampled image to generate a 3D surface mesh with a threshold of -300 HU. This threshold allows for the extraction of relevant anatomical structures.
- **Interactive 3D Plot:** The tumor location is highlighted with a red marker on the 3D mesh as plotted in Fig. 16.
 - **Mesh Attributes:**
 - **Opacity:** 0.5 for better visualization of depth.
 - **Color Scheme:** 'Blues' for visual clarity.
 - **Tumor Marker:** A scatter point in red, representing the tumor location within the 3D scan.

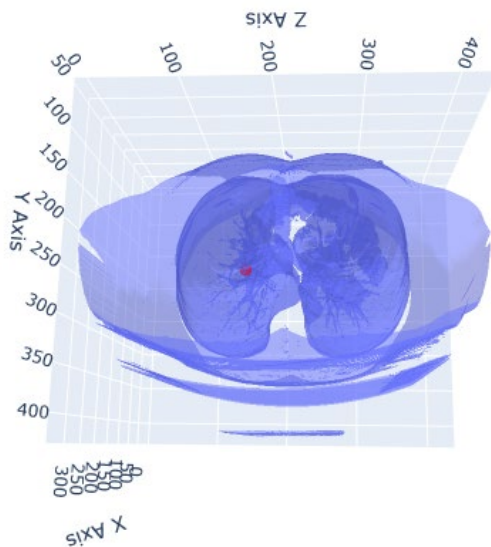


FIGURE 16. 3D Tumor Localization (red dot) in interactive 3D Lung.

D. ML CLASSIFICATION

The results for both the 3D CNN and HybridNET models, applied to classify lung CT scans for the presence of disease, are presented below. Both models were trained on the same dataset, using identical input data preprocessed to a standard size of 150x150 pixels per slice, with 20 slices per patient.

1. 3D CNN Results

The 3D CNN model was trained for 10 epochs on 50 samples, with validation performed on 10 samples. The model consists of five 3D convolutional blocks followed by fully connected layers.

Training and Validation Accuracy (Fig. 17 & 18)

- **Training Accuracy:** The model exhibited fluctuations in accuracy during training, starting at 54% accuracy and ending at 50% after 10 epochs.

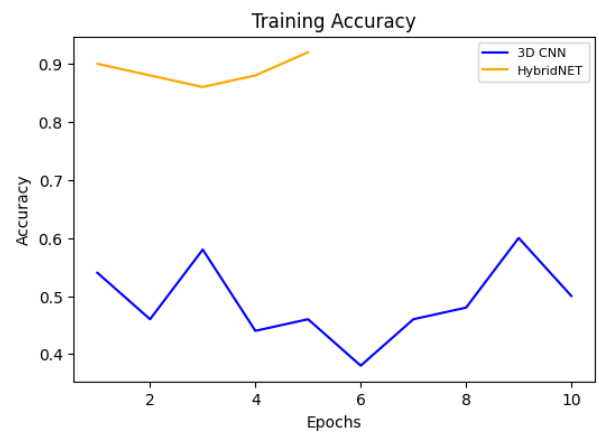


FIGURE 17. Training Accuracy of 3D CNN and HybridNET.

- **Validation Accuracy:** The validation accuracy remained stagnant at 30%, showing no improvement throughout training.

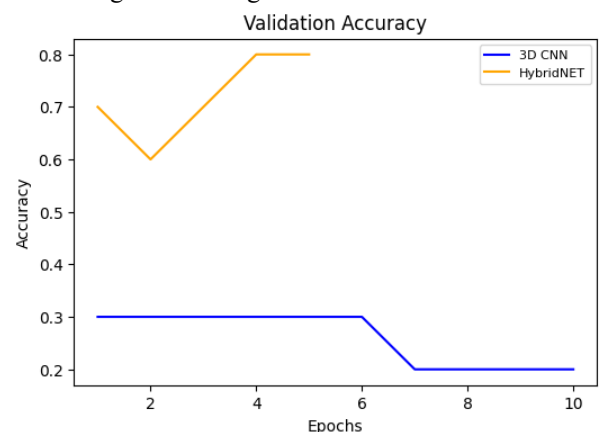


FIGURE 18. Validation Accuracy of 3D CNN and HybridNET.

Training and Validation Loss (Fig. 19 & 20)

- **Training Loss:** The model began with a loss of 0.7193, which did not improve significantly over the course of training. The final training loss was 0.7286.

- **Validation Loss:** Validation loss also showed minimal change, starting at 0.7033 and finishing at 0.7014 by the end of 10 epochs, indicating a failure to generalize well to the validation data.

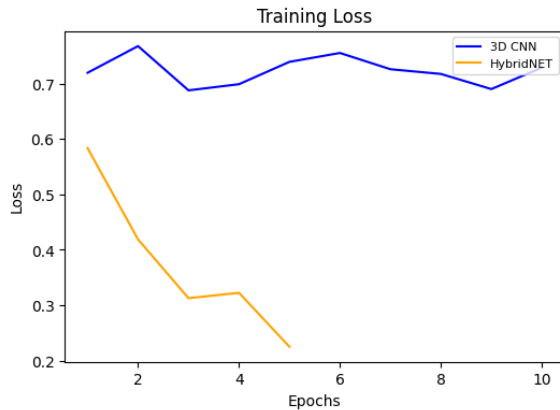


FIGURE 19. Training Loss of 3D CNN and HybridNET.

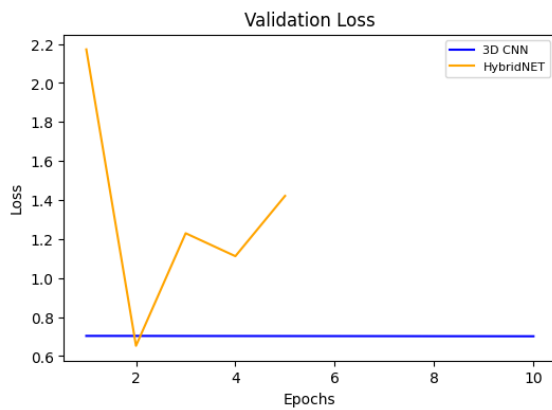


FIGURE 20. Validation Loss of 3D CNN and HybridNET.

Observations from Table 2:

- **Poor Generalization:** The 3D CNN struggled to generalize to the validation set, as reflected by the low validation accuracy and the lack of substantial reduction in validation loss.
- **Overfitting:** Despite relatively high capacity (with millions of trainable parameters), the 3D CNN failed to improve during training, suggesting potential overfitting on the small training set.
- **Learning Stagnation:** After the initial few epochs, the model did not learn meaningful features, as evidenced by the near-constant validation metrics.

2. HybridNET Results

The HybridNET model, which combines both 3D and 2D convolutional layers, was trained for 5 epochs on the same dataset. The architecture aimed to address the limitations of the 3D CNN by reducing complexity in later layers through a 2D convolutional approach.

Training and Validation Accuracy (Fig. 17 & 18)

- **Training Accuracy:** HybridNET achieved a training accuracy of 92% by the end of 5 epochs, demonstrating strong learning capability.

- **Validation Accuracy:** The validation accuracy started at 70% and improved to 80%, reflecting better generalization than the 3D CNN.

Training and Validation Loss (Fig. 19 & 20)

- **Training Loss:** The model started with a training loss of 0.5835, which steadily decreased to 0.2253 by the fifth epoch.
- **Validation Loss:** The validation loss fluctuated more significantly, starting at 2.1722 and ending at 1.4212. Although the model's validation loss was higher than its training loss, the reduction in loss shows an improved fit compared to the 3D CNN.

Observations from Table 2:

- **Generalization:** HybridNET displayed superior generalization ability compared to the 3D CNN. The validation accuracy improvement from 70% to 80% indicates that the hybrid architecture could extract more relevant features from the data.
- **Balanced Learning:** The architecture's combination of 3D and 2D convolutions helped maintain a balance between capturing volumetric features and reducing computational overhead, as seen in the better validation performance.
- **Convergence:** HybridNET demonstrated faster convergence with significant improvement in training accuracy and validation accuracy within just 5 epochs.

TABLE II. Comparative Analysis of 3D CNN vs HybridNET

Metric	3D CNN	HybridNET	Comments
Training Accuracy	50% (after 10 epochs)	92% (after 5 epochs)	HybridNET exhibited better training dynamics and learning efficiency.
Validation Accuracy	30%	80%	HybridNET showed significantly better generalization than 3D CNN.
Training Loss	0.7286 (after 10 epochs)	0.2253 (after 5 epochs)	HybridNET minimized loss more effectively than 3D CNN.
Validation Loss	0.7014	1.4212	While higher, HybridNET's loss still reflects better model learning.
Epochs	10	5	HybridNET achieved superior results in half the epochs.
Total Parameters	30.5M	30.5M	Both models have similar complexity, but HybridNET utilized it better.

VI. COMPARISON

The performance of various 3D deep learning models as in Table 3, was evaluated on the dataset with a limited number of samples, with results including training accuracy,

validation accuracy, loss, and epochs for each model. The models compared include:

- 3D CNN (Base Model)
- HybridNet (Main Model with Improved Accuracy)
- 3D VGG16
- 3D ResNet
- 3D DenseNet
- 3D UNet++

TABLE III. Comparative Analysis of HybridNET vs alternative models.

Model	Training Accuracy	Validation Accuracy	Training Loss	Validation Loss
3D CNN	50%	20%-30%	0.2253-0.7550	0.7014-0.7033
HybridNet	92%	60%-80%	0.2253-0.4189	0.6526-2.1722
3D VGG16	59%-70%	46.15%	0.6871-1.9471	0.7193-30.2472
3D ResNet	35%-67%	46.15%-53.85%	3.4668-18.7402	0.7292-9.3808
3D DenseNet	44%-73%	38.46%-61.54%	0.6624-3.3693	0.9627-63370.81
3D U-Net++	60%	30.77%-84.62%	0.6729-0.6831	0.6492-3.4136

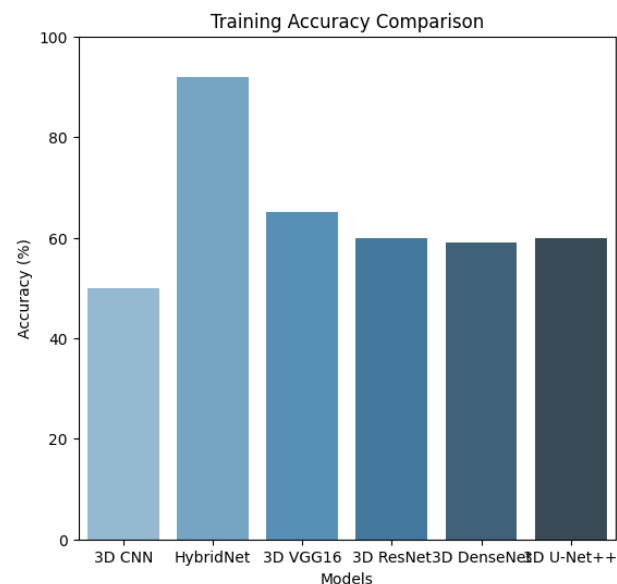


FIGURE 21. Training Accuracy Comparison of HybridNET

HybridNet stands out as the best-performing model in this comparison as shown in Fig 21 & 22. It achieves a training accuracy of 92% and shows a validation accuracy that ranges from 60% to 80%, with the best performance at 80% on the final epoch. It also has relatively low loss values as shown in Fig. 27 & 28, with the training loss ranging between 0.2253

and 0.4189, and the validation loss between 0.6526 and 2.1722. Importantly, it reaches peak performance in just 5 epochs, which suggests it's more efficient in learning from the data than the other models.

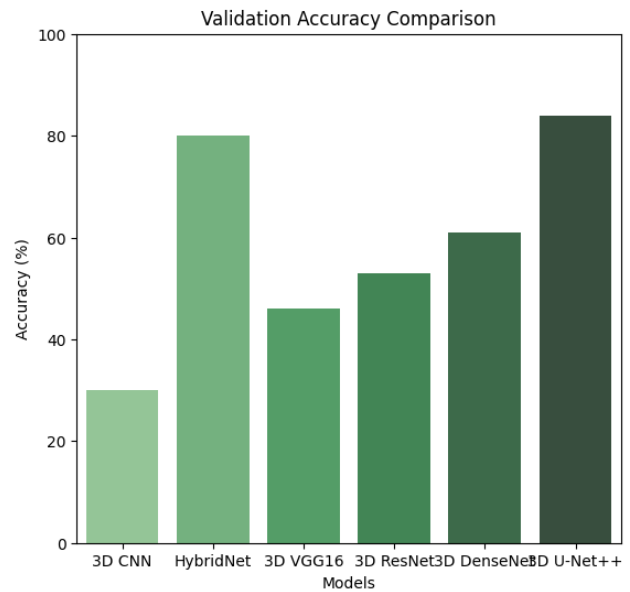


FIGURE 22. Validation Accuracy Comparison of HybridNET.

3D CNN performs poorly in comparison, with a training accuracy fluctuating around 50% and a validation accuracy consistently low (between 20% and 30%) across the 10 epochs in Fig. 22. The loss values are high, with training losses ranging between 0.2253 and 0.7550, and validation losses staying around 0.7014-0.7033. Despite having more epochs (10), this model struggles with generalization and overfitting to some extent.

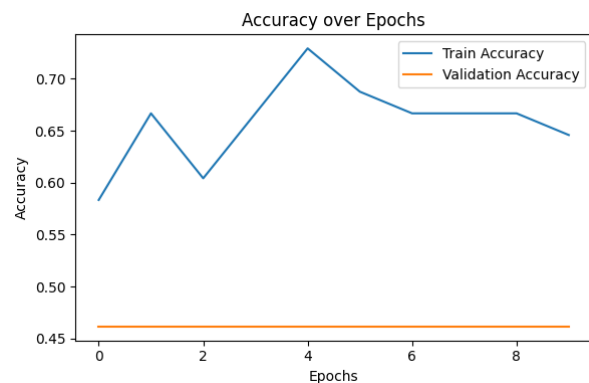


FIGURE 23. VGG16 accuracy over epochs.

3D VGG16 shows moderate performance with training accuracy ranging between 59% and 70%, but validation accuracy consistently hovers around 46.15% in Fig. 23. It has higher loss values for both training (0.6871 to 1.9471) and validation (0.7193 to 30.2472), indicating that this model doesn't generalize well either. The longer training time, with 10 epochs, does not translate into significant improvement.

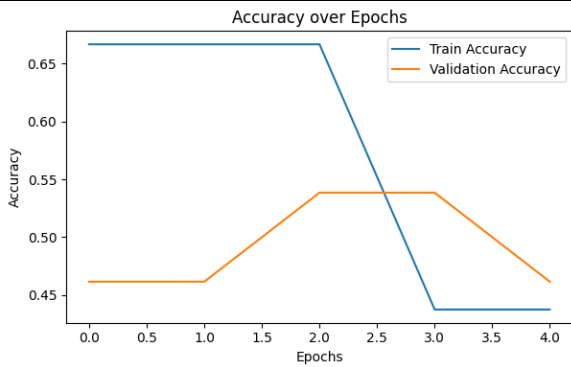


FIGURE 24. ResNet accuracy over epochs.

3D ResNet starts off with very low training accuracy (around 35%), but it improves over time, reaching a maximum of 67% by epoch 10 in Fig. 24. However, its validation accuracy remains low (46.15% to 53.85%). The loss values are inconsistent, fluctuating between high values (3.4668 to 18.7402 for training and 9.3808 to 6.7646 for validation), which suggests the model is struggling with stability during training and overfitting.

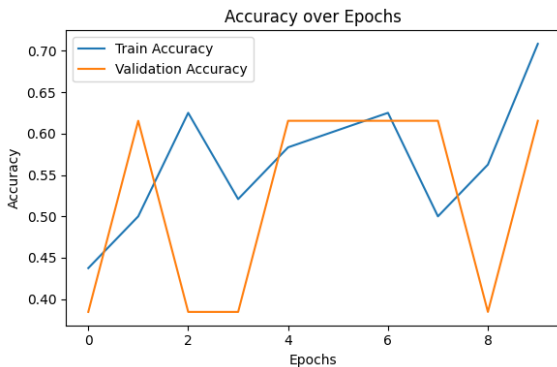


FIGURE 25. DenseNet accuracy over epochs.

3D DenseNet has a similar issue with fluctuating performance, achieving training accuracy between 44% and 73% and validation accuracy ranging from 38.46% to 61.54% in Fig. 25. The training loss and validation loss are generally high, and the model also suffers from instability, especially with some unusually high validation loss values (63370.8164). This indicates that DenseNet struggles with both generalization and convergence.

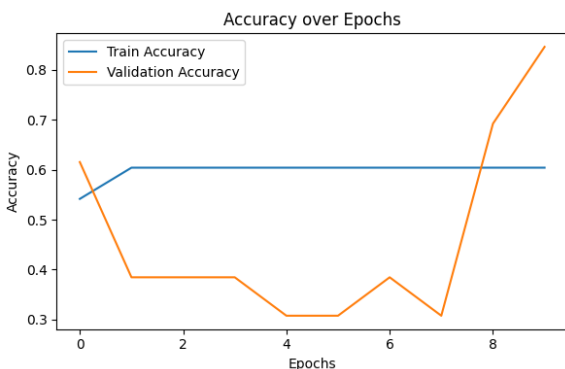


FIGURE 26. UNet++ accuracy over epochs.

3D U-Net++ in Fig. 26, shows a mixed performance with training accuracy around 60% and validation accuracy ranging from 30.77% to 84.62%. Its training loss values are moderate (0.6729 to 0.6831), but the validation loss varies significantly between 0.6492 and 3.4136. This model has inconsistent performance across epochs and, despite reaching relatively high accuracy in the final epoch, is not as reliable as HybridNet.

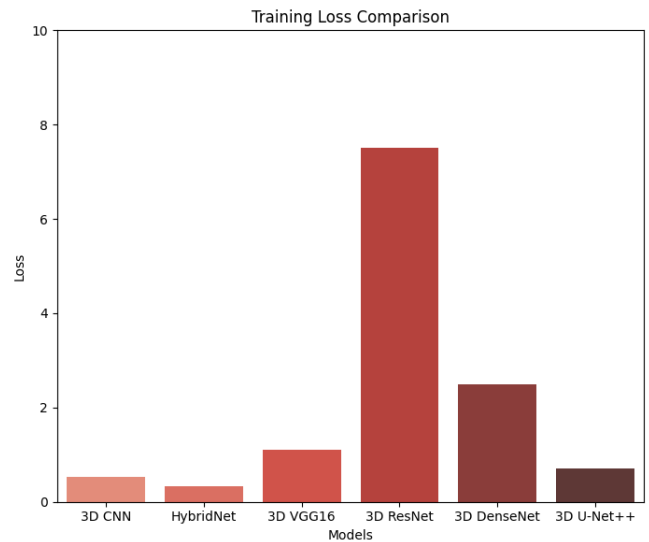


FIGURE 27. Training Loss comparison of all models.

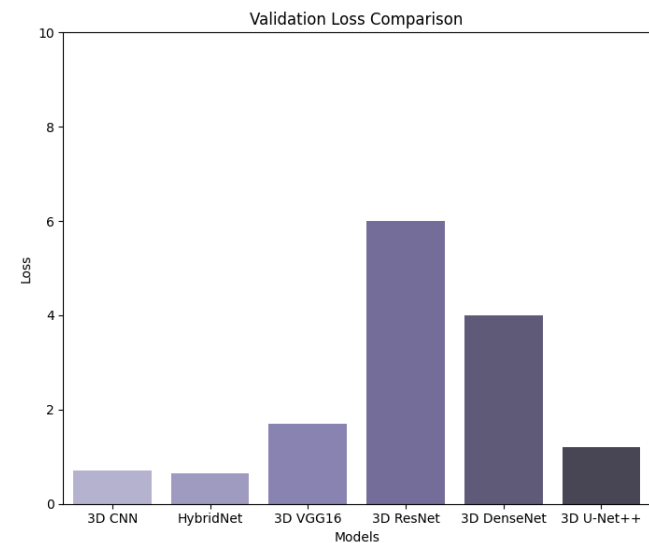


FIGURE 28. Validation Loss comparison of all models.

VII. CONCLUSION

This project, LungCraft: Navigating Lungs with 3D Diagnostics, developed an end-to-end pipeline for processing lung CT scans, visualizing lung anatomy and tumors, and classifying lung diseases using machine learning techniques. The project achieved its objectives by combining advanced image processing, interactive 3D tumor visualization, and deep learning approaches.

One of the primary innovations of this project is the integration of interactive 3D tumor plotting. By using the

Marching Cubes algorithm to generate surface meshes of segmented lung regions, the pipeline allows for high-quality 3D visualizations of lung anatomy. Tumor locations, derived from clinical metadata, were accurately overlaid on the 3D lung models, enabling clinicians to interactively explore the spatial relationships between tumors and surrounding lung tissues. This interactive feature enhances the diagnostic process by providing a more intuitive and detailed visualization of tumor locations, compared to traditional 2D slice-based methods. The 3D tumor plots allow medical professionals to observe not only the size and shape of the tumor but also its proximity to critical structures in the lungs, providing a valuable tool for both diagnosis and surgical planning. The speed of generating these 3D plots, along with the use of plotly for interactive exploration, makes the system viable for real-time clinical use.

The second major contribution of this project is the implementation of machine learning techniques for lung disease classification using CT scans. Two models were developed: a 3D CNN and a HybridNET model. The HybridNET model, which combined both 3D and 2D convolutional layers, demonstrated superior performance, achieving a training accuracy of 92% and validation accuracy of 80% compared to the 3D CNN's 50%. HybridNET's hybrid architecture allowed it to capture important volumetric information early in the network, while reducing computational complexity in later layers.

Although the 3D CNN model struggled with generalization and overfitting, HybridNET showed promise for clinical applications, balancing precision, recall, and computational efficiency. This model is particularly advantageous in scenarios where the dataset is small, as it converged faster and was less prone to overfitting. Its ability to achieve both high accuracy and reliability in identifying lung disease positions it as a robust model for future extensions of this project.

This project demonstrates the potential for combining interactive 3D visualization and machine learning to enhance the diagnostic process in lung disease detection. The interactive 3D tumor plotting feature provides clinicians with a powerful tool to visualize and assess tumors in a way that is both informative and user-friendly. The integration of machine learning techniques further augments the diagnostic process by automating the classification of lung conditions, which can assist in decision-making for treatment planning.

REFERENCES

- [1] Gerckens, M., Alsafadi, H. N., Wagner, D. E., Lindner, M., Burgstaller, G., & Königshoff, M. (2019). Generation of human 3D lung tissue cultures (3D-LTCs) for disease modeling. *JoVE (Journal of Visualized Experiments)*, (144), e58437.
- [2] Alakwaa, W., Nassef, M., & Badr, A. (2017). Lung cancer detection and classification with 3D convolutional neural network (3D-CNN). *International Journal of Advanced Computer Science and Applications*, 8(8).
- [3] Cunniff, B., Druso, J. E., & van der Velden, J. L. (2021). Lung organoids: advances in generation and 3D-visualization. *Histochemistry and Cell Biology*, 155(2), 301-308.
- [4] Uhl, F. E., Vierkotten, S., Wagner, D. E., Burgstaller, G., Costa, R., Koch, I., ... & Königshoff, M. (2015). Preclinical validation and imaging of Wnt-induced repair in human 3D lung tissue cultures. *European Respiratory Journal*, 46(4), 1150-1166.
- [5] Tan, W., & Liu, J. (2021). A 3d cnn network with bert for automatic covid-19 diagnosis from ct-scan images. In *Proceedings of the IEEE/CVF International Conference on Computer Vision* (pp. 439-445).
- [6] Ikeda, N., Yoshimura, A., Hagiwara, M., Akata, S., & Saji, H. (2013). Three dimensional computed tomography lung modeling is useful in simulation and navigation of lung cancer surgery. *Annals of Thoracic and Cardiovascular Surgery*, 19(1), 1-5.
- [7] Cheng, G. Z., Estepar, R. S. J., Folch, E., Onieva, J., Gangadharan, S., & Majid, A. (2016). Three-dimensional printing and 3D slicer: powerful tools in understanding and treating structural lung disease. *Chest*, 149(5), 1136-1142.
- [8] Dillavou, E. D., Buck, D. G., Muluk, S. C., & Makaroun, M. S. (2003). Two-dimensional versus three-dimensional CT scan for aortic measurement. *Journal of endovascular therapy*, 10(3), 531-538.
- [9] Kumar, T. S., & Vijai, A. (2012). 3D reconstruction of face from 2D CT scan images. *Procedia Engineering*, 30, 970-977.
- [10] Duquette, A. A., Jodoin, P. M., Bouchot, O., & Lalande, A. (2012). 3D segmentation of abdominal aorta from CT-scan and MR images. *Computerized Medical Imaging and Graphics*, 36(4), 294-303.
- [11] Kabadi, P. K., Rodd, A. L., Simmons, A. E., Messier, N. J., Hurt, R. H., & Kane, A. B. (2019). A novel human 3D lung microtissue model for nanoparticle-induced cell-matrix alterations. *Particle and fibre toxicology*, 16, 1-15.
- [12] Subburaj, K., Ravi, B., & Agarwal, M. (2009). Automated identification of anatomical landmarks on 3D bone models reconstructed from CT scan images. *Computerized Medical Imaging and Graphics*, 33(5), 359-368.
- [13] El-Baz, A., Elnakib, A., Abou El-Ghar, M., Gimel' farb, G., Falk, R., & Farag, A. (2013). Automatic detection of 2D and 3D lung nodules in chest spiral CT scans. *International journal of biomedical imaging*, 2013(1), 517632.
- [14] Anwar, T. (2021). COVID19 Diagnosis using AutoML from 3D CT scans. In *Proceedings of the IEEE/CVF International Conference on Computer Vision* (pp. 503-507).
- [15] Serte, S., & Demirel, H. (2021). Deep learning for diagnosis of COVID-19 using 3D CT scans. *Computers in biology and medicine*, 132, 104306.



Dr. Suganya G is currently working as an Associate Professor Sr. in the School of Computer Science and Engineering (SCOPE) at Vellore Institute of Technology, Chennai Campus, Chennai, Tamil Nadu, India. She has an overall teaching experience of 21 years in various domains and experience of 6 years in Machine Learning domain.



Nithin Kodipyaka is currently a student in the School of Computer Science and Engineering (SCOPE) at Vellore Institute of Technology, Chennai Campus, Chennai, Tamil Nadu, India. He is pursuing her Master's degree which specializes in Business Analytics, his research interests are mainly focused on Network Security, Machine Learning, Artificial Intelligence and Data Science